

X-ray Intraday Variability and Power Spectral Density Profiles of the Blazar 3C 273 with *XMM-Newton* during 2000 – 2021

G. S. Pavana Gowtami^{1*}, Haritma Gaur^{2†}, Alok C. Gupta^{2‡§}, Paul J. Wiita³, Mai Liao^{4,5},

Martin Ward⁶

¹*Department of Physics, Indian Institute of Technology (IIT) Bombay, Powai, Mumbai – 400076, India*

²*Aryabhata Research Institute of Observational Sciences (ARIES), Manora Peak, Nainital – 263001, India*

³*Department of Physics, The College of New Jersey, 2000 Pennington Rd., Ewing, NJ 08628-0718, USA*

⁴*CAS Key Laboratory for Researches in Galaxies and Cosmology, Department of Astronomy, University of Science and Technology of China, Hefei, Anhui 230026, China*

⁵*School of Astronomy and Space Science, University of Science and Technology of China, Hefei, Anhui 230026, China*

⁶*Centre for Extragalactic Astronomy, Department of Physics, University of Durham, South Road, Durham DH1 3LE, UK*

31 January 2022

ABSTRACT

We present X-ray intraday variability and power spectral density (PSD) analyses of the longest 23 pointed *XMM-Newton* observations of the blazar 3C 273 that were taken during 2000 – 2021. These good time intervals contained between 5 and 24.6 hours of data. Variability has been estimated in three energy bands: 0.2 – 2 keV (soft), 2 – 10 keV (hard), and 0.2 – 10 keV (total). Nine of the 23 observations exhibited some variability, though no major variations exceeding 5 per cent were detected. Typical timescales for variability were ~ 1 ks. For those variable light curves we find that a power-law model provides good fits to each PSD, with most of the slopes between -1.7 and -2.8 . Although no variations of hardness ratio could be measured in any individual observation, an anti-correlation in flux and hardness ratio is found in long term data that indicates a harder when brighter trend. Our flux and spectral analyses indicate that both particle acceleration and synchrotron cooling processes make an important contribution to the emission from this blazar.

Key words: galaxies: quasars: general – quasars: individual: 3C 273 – radiation mechanisms: non-thermal

1 INTRODUCTION

Super massive black holes (SMBHs) in the mass range $\sim 10^6 - 10^{10} M_{\odot}$ are present at the center of active galactic nuclei (AGN) which accrete matter from their surroundings and emit both thermal and non-thermal radiation. A large fraction of AGN, $\sim 85 - 90$ %, either emit very little or almost no radiation in radio bands and are called radio quiet (RQ) AGN, but the remaining $\sim 10 - 15$ % emit strongly in radio bands and are known as radio loud (RL) AGN (Kellermann et al. 1989). A standard AGN classification is based on the importance of relativistic jet emission, in which RQAGN lack significant relativistic jets while RLAGN have strong relativistic jets (Padovani 2017).

Blazars are a subclass of RLAGN in which a powerful relativistic jet is closely aligned to the observer’s line of site (Urry & Padovani 1995). BL Lacertae objects and flat spectrum radio

quasars (FSRQs) are collectively known as these blazars. In the composite optical/UV spectrum, BL Lacertae objects show either featureless or only very weak emission lines (equivalent width $EW \leq 5\text{\AA}$) (Stoeckel et al. 1991; Marcha et al. 1996) while FSRQs have prominent emission lines (Blandford & Rees 1978; Ghisellini et al. 1997). In the present age of multi-wavelength (MW) transient astronomy, blazars are among one of the most well studied astronomical transients, because they emit radiation across the complete electromagnetic (EM) spectrum, their fluxes and polarizations are highly variable, and this emission is predominantly non-thermal. Since blazars emit radiation from the whole EM spectrum, their MW spectral energy distributions (SEDs) can be studied. Blazars’ SEDs evince a double-hump structure in which the first hump (lower energy) peaks somewhere between infrared (IR) and X-ray energies and the emission is dominated by synchrotron radiation from the relativistic jet, while the second hump (higher energy) located in GeV to TeV γ -rays energies can be produced by various leptonic and/or hadronic-based emission processes (e.g. Kirk et al. 1998; Mücke et al. 2003; Krawczynski 2004; Gaur et al. 2010).

Blazar flux variations in all EM bands range over all observable time scales ranging from a few minutes to several decades.

* Email: g.pavana.s.gowtami7@gmail.com

† Email: harry.gaur31@gmail.com

‡ Email: acgupta30@gmail.com

§ Corresponding Author

Flux variability detected in blazars on time scales of a few minutes to less than a day is often known as intra-day variability (IDV) (Wagner & Witzel 1995); variations in flux from days to a few months are commonly known as short-term variability (STV); while the flux variations over longer timescales are often called long-term variability (LTV) (e.g., Gupta et al. 2004).

3C 273¹ ($\alpha_{2000} = 12^{\text{h}} 29^{\text{m}} 06.698^{\text{s}}$; $\delta_{2000} = +02^{\circ} 03' 08.58''$) at $z = 0.1575$ is the first discovered quasar (Schmidt 1963). It belongs to the FSRQ class of blazar and knots in its jet show apparent superluminal motion (Jorstad et al. 2001, 2005). 3C 273 has an additional “big blue bump” (BBB) which dominates the optical through soft X-ray emission (Paltani et al. 1998). It is generally agreed that the BBB comes from more nearly isotropic emission from the close vicinity of the central SMBH, presumably from the accretion disc (Kataoka et al. 2002). 3C 273 is among the most extensively studied blazars across the complete EM spectrum on diverse timescales. Observations have been carried out in single bands as well as in MW campaigns (simultaneous and/or non-simultaneous) (e.g., Collmar et al. 2000; Romero et al. 2000; Sambruna et al. 2001; Courvoisier et al. 2003; Paltani & Türler 2005; Attridge et al. 2005; Savolainen et al. 2006; Uchiyama et al. 2006; Soldi et al. 2008; Fan et al. 2009; Abdo et al. 2010; Fan et al. 2014; Kalita et al. 2015; Chidiac et al. 2016; Kalita et al. 2017; Liu et al. 2019; Carini et al. 2020; Fernandes et al. 2020, and references therein).

Focusing on X-ray observations, a ~ 18 ks integration of 3C 273 in January 1992 with *ROSAT HRI*, clearly detected a X-ray jet all along the optically visible jet as well as a faint X-ray halo with a characteristic scale of 29 kpc (Röser et al. 2000). Sambruna et al. (2001) reported *Chandra* observations of the X-ray jet of 3C 273 during the calibration phase in 2000 January. They detected the brightest optical knots in the 0.2 – 8 keV energy band and found that the X-ray morphology nicely tracks that of the optical. By using five observations of 3C 273 with *Chandra*, at least four distinct features were resolved in the jet, and it was found that the X-ray emission mostly arises from the “inner jet” between 5'' and 10'' from the core (Marshall et al. 2001). A deep *Chandra* observation of the high-powered FSRQ jet, along with radio and optical measurements, showed that the X-ray spectra were much softer than the radio spectra in all regions of the bright part of the jet, except for the first bright “knot A”. These observations ruled out a model in which the X-ray emission from the entire jet arises from beamed inverse Compton (IC) scattering of cosmic microwave background photons in a single-zone jet flow (Jester et al. 2006). It has been suggested that the X-ray and γ -ray fluxes from “knot A” may have a common origin in synchrotron emission from the accelerated protons (Kundu & Gupta 2014). Combined temporal and spectral analyses of 3C 273 suggest that a two-component model is needed to explain the complete high energy spectrum, where X-ray emission is likely to be dominated by a Seyfert-like component while the γ -ray emission is dominated by a blazar-like component produced by the relativistic jet (Esposito et al. 2015).

The FeK α line is an important physical diagnostic in X-ray spectra of AGNs and quasars but has been extremely difficult to measure in the blazar 3C 273. Nonetheless, it has been detected occasionally in 3C 273. Yaqoob & Serlemitsos (2000) detected strong Fe K α line from a 1996 July observing campaign of 3C

273 with *RXTE* and *ASCA*, and another detection could be made from all the data on the blazar taken by *ASCA* from 1993 – 2000. In a *XMM-Newton* observation taken on 7 July 2003 (Obs ID 159960101, see Table 1) the FeK α line also was detected (Kalita et al. 2017). The FeK α line is generally seen in Seyfert 1 galaxies from which it can be concluded that the X-ray emission from 3C 273 is a mixture of a thermal AGN component associated with the inner accretion flow emission from the disc’s corona as well as non-thermal processes produced in the jet component (Magdziarz & Zdziarski 1995).

Some of the most puzzling flux variations are those happening on IDV timescales. Study of IDV is an important method for learning about structures on small spatial scales, and also provides us with better understanding of the different radiation mechanisms that are important in the emitting regions in the vicinity of the central engine of blazars (Wagner & Witzel 1995). To better understand blazars’ flux variabilities on IDV timescales, over the past decade and more, we have been using public archive data of blazars taken from various X-ray satellites (e.g. *XMM-Newton*, *NuStar*, *Chandra*, and *Suzaku*). We reported these results in a series of papers (Lachowicz et al. 2009; Gaur et al. 2010; Bhagwan et al. 2014, 2016; Kalita et al. 2015; Gupta et al. 2016; Pandey et al. 2017, 2018; Aggrawal et al. 2018; Zhang et al. 2019, 2021; Dhiman et al. 2021). In a sample of 24 *XMM-Newton* LCs of 4 high energy peaked blazars (PKS 0548–322, ON 231, 1ES 1426+428, and PKS 2155–304), a ~ 4.6 hour quasi periodic oscillation (QPO) was detected in a 0.3 – 10 keV LC of PKS 2155–304 (Lachowicz et al. 2009), and possible weak QPOs may have been present in LCs of ON 231 and PKS 2155–304. IDV timescales ranging from 15.7 to 46.8 ks were present in eight of their LCs (Gaur et al. 2010). By using 20 *XMM-Newton* pointed observations of PKS 2155–304 with simultaneous X-ray and UV/optical data, spectral energy distributions (SEDs) were constructed and fitted with a combined power-law and log-parabolic model (Bhagwan et al. 2014). Three continuous pointings of ~ 92 ks of PKS 2155–304 on 24 May 2002 with *XMM-Newton* displayed a mini-flare, a nearly constant flux period and a strong flux increase (Bhagwan et al. 2016). Two dozen pointed X-ray observations of the low energy peaked blazar 3C 273 taken during 2000 – 2012 with *XMM-Newton* displayed occasionally very low amplitude flux variation (Kalita et al. 2015) and here we expand upon that work.

In an extensive X-ray IDV study of the 12 low energy peaked blazars involving 50 observations from *XMM-Newton* since its launch to 2012, it was found that this class is not very variable in these X-ray bands, with a duty cycle ~ 4 per cent (Gupta et al. 2016). An examination of 46 LCs taken with the *Nuclear Spectroscopic Telescope Array* (*NuSTAR*) of 11 TeV emitting blazars, found that 6 of these blazars exhibited IDV in the *NuSTAR* energy range of 3 – 79 keV (Pandey et al. 2017, 2018). An extensive study of 72 *Chandra* LCs of the TeV blazar Mrk 421 between 2000 and 2015, showed that this source often displayed IDV in the energy range 0.3 – 10.0 keV with duty cycle of ~ 84 per cent (Aggrawal et al. 2018). In 16 pointed observations of the TeV blazars Mrk 421 and PKS 2155–304 taken during the whole operational period of *Suzaku*, large amplitude IDV was seen every time (Zhang et al. 2019, 2021). In a recent study of twenty pointed *XMM-Newton* observations of the TeV blazar PG 1553+113 taken during 2010 – 2018, IDV was seen in the X-ray energy range (0.3 – 10 keV) in 16 out of 19 LCs, or a duty cycle of $\sim 84\%$ (Dhiman et al. 2021).

¹ <https://www.lsw.uni-heidelberg.de/projects/extragalactic/charts/1226+023.html>

In blazars, IDV across the complete EM spectrum is usually dominated by radiation changes intrinsic to the source, except for low-frequency radio observations that may include fluctuations of extrinsic origin arising from interstellar scintillation (e.g. [Wagner & Witzel 1995](#)). The bulk of the intrinsic flux variability in blazars at all wavelengths, including X-rays, can be explained by the relativistic shock-in-jet based radio loud AGN emission models, particularly those that include relativistic turbulence or magnetic reconnection in the jets that can produce the fast IDV (e.g., [Marscher & Gear 1985](#); [Gopal-Krishna & Wiita 1992](#); [Marscher 2014](#); [Calafut & Wiita 2015](#); [Pollack et al. 2016](#); [Zhang & Giannios 2021](#); [Borse et al. 2021](#), and references therein). In other classes of AGNs and for blazars in low-flux states, variations in optical and UV emission can be explained with accretion disc models (e.g., [Mangalam & Wiita 1993](#); [Chakrabarti & Wiita 1993](#)) where the X-rays arise from the disc corona ([Soldi et al. 2008](#); [Buisson et al. 2017](#); [Liu et al. 2021](#)). In the case of 3C 273, it has long been argued that there are substantial contributions from both the disc and the jet in both optical ([Impey et al. 1989](#); [Paltani et al. 1998](#)) and X-ray bands ([Grandi & Palumbo 2004](#)). Recently, [Li et al. \(2020\)](#) have shown that the jet contribution to the optical emission of 3C 273 ranges between 10 and 40 per cent, with a mean of ~ 28 per cent.

For the present work, we have taken public archive data of the blazar 3C 273 taken by the EPIC-pn instrument on board the *XMM-Newton* satellite. There are a total of 23 pointed observations which have qualified under our selection criteria described in Section 2. These observations were carried out for a period spanning just over 21 years (2000 – 2021). The data we discuss here are very useful to study flux variability, power density spectra and spectral variations on IDV timescales. This study should help us to understand the X-ray properties of this blazar on the smallest physical scales.

The paper is arranged as follows. In Section 2, we discuss the *XMM-Newton* public archive data of the blazar 3C 273 and how we reduced it. Section 3 provides brief descriptions of the various analysis techniques we have used. In Section 4 the results are presented. We present a discussion and conclusions in sections 5 and 6, respectively.

2 XMM-NEWTON ARCHIVAL DATA SELECTION AND REDUCTION

2.1 Data selection parameters

In this work we consider the FSRQ 3C 273, which was continuously monitored for extended periods of time by the *XMM-Newton* satellite on many occasions since its launch until June 2021. We took only the X-ray data from the European Photon Imaging Camera (EPIC)-pn detector from the online *XMM-Newton* public archive². We did not incorporate EPIC-MOS (Metal Oxide Silicon) instrument data for the present study. The path of EPIC-MOS instruments is partially obscured by the RGS (Reflection Grating Spectrometer) instruments for focussing the incoming photons of the interested source so that the effective area of both EPIC-MOS 1 and MOS 2 is less than that of the EPIC-pn. In addition, the effective area of the EPIC-MOS decreases rapidly with respect to the EPIC-pn instrument above an energy of ~ 4 keV. Another

important reason for preferring the EPIC-pn data is that has timing resolution almost 50 times higher compared to EPIC-MOS³. We therefore preferred EPIC-pn data sets to study the variability properties of the object. We note that for similar earlier studies, we have only used EPIC-pn data (e.g., [Gaur et al. 2010](#); [Bhagwan et al. 2014](#); [Gupta et al. 2016](#); [Dhiman et al. 2021](#), and references therein).

The data, which consist of 43 pointed observations, were taken from 13 June 2000 to 9 June 2021, spanning almost exactly 21 years. We immediately eliminated 11 observations of which 1 does not have PN data while another 10 have few data points. Nine more observations are excluded as they have a good time interval (GTI) of less than 18 ks, or 5 hours. Our analysis is performed on the 23 remaining Obs IDs. A summary of the 3C 273 public archive data we used is given in Table 1.

2.2 Data Reduction

The onboard system of *XMM-Newton* satellite consists of two CCDs, the MOS and PN cameras. As noted above, only the EPIC-pn data are considered here as they have higher count rates and more high energy sensitivity than MOS data; they also have less pile-up distortion (e.g. [González-Martín & Vaughan 2012](#)). The EPIC-pn camera takes the image of the target in the energy range of 0.15 – 15 keV in the X-ray band. However, the data above 10 keV is dominated by strong proton flaring. The on-axis effective area of the EPIC-pn camera reflects X-ray photons most efficiently at 0.2 to 10 keV. So to obtain high quality datasets, we consider the 0.2 – 10 keV X-ray energy range.

We processed this data using the standard procedure of the *XMM-Newton* Science Analysis System (SAS) version 19.0.0 with the most recent available Current Calibration File⁴. The event files of the PN detector were generated through *epproc*. Before generating a cleaned event list, we first examined the light curve (LC) in the energy range 10 – 12 keV to find the soft proton flares. To remove them, a good time interval (GTI) file using the *tabgtigen* tool is generated which contains information of the time intervals free from these flares. In the next step, we used the event list file and GTI files as input to obtain cleaned event files using the *evselect* tool. Then, filtering of the data is done using the condition ($PATTERN \leq 4$) and ($FLAG = 0$) in 3 different energy bands: total (0.2 – 10 keV), soft (0.2 – 2 keV) and hard (2 – 10 keV). The source counts are normally taken from a circular aperture of radius of 40 arcseconds and the background counts were found by taking a circular region that ranged between 40 and 50 arcsec radius for different images/CCD chips, always as far away as possible from the source on the same CCD chip. Any pile-up is detected using the *epatplot* routine. The pile-up is removed by selecting a central annulus region instead of circular region for the source event file. All observations are binned at 100 seconds. By subtracting the background counts from the source counts, the final corrected events are obtained using the *epiclccorr* task. High background periods at the beginning and end of some of the observations were removed to obtain the final corrected lists.

The 23 publicly archived pointed *XMM-Newton* observations of the FSRQ blazar 3C 273 we analyzed have individual GTIs

² HEASARC (High-Energy Astrophysics Science Archive Research Centre)

³ https://xmm-tools.cosmos.esa.int/external/xmm_user_support/documentation/uhb/effarea

⁴ <http://www.cosmos.esa.int/web/xmm-newton/sas-threads> (I. de la Calle)

Table 1. Observation log of *XMM-Newton* X-ray data for 3C 273.

ObsID	Date of Obs. yyyy.mm.dd	Revolution	GTI ^a (ks)	Pileup	$\mu(\text{counts/s})^b$			Mean HR
					Soft (0.2–2 keV)	Hard (2–10 keV)	Total (0.2–10 keV)	
0126700301	2000.06.13	94	64.9	no	42.16±0.83	9.88±0.40	51.93±0.92	−0.62±0.01
0126700601	2000.06.15	95	29.6	no	40.53±0.81	9.68±0.40	50.10±0.90	−0.61±0.01
0126700701	2000.06.15	95	29.9	no	39.32±0.80	9.43±0.39	48.65±0.89	−0.61±0.01
0126700801	2000.06.17	96	56.5	no	39.53±0.80	9.43±0.39	48.85±0.89	−0.61±0.01
0136550101	2001.06.13	277	88.6	no	55.68±0.95	11.75±0.44	67.30±1.05	−0.65±0.01
0159960101	2003.07.07	655	58.1	yes	86.87±3.99	15.67±1.70	102.54±4.34	−0.69±0.03
0136550801	2004.06.30	835	18.0	no	39.87±0.81	8.34±0.37	48.12±0.89	−0.65±0.01
0136551001	2005.07.10	1023	27.6	no	42.97±0.82	10.05±0.40	52.92±0.91	−0.62±0.01
0414190101	2007.01.12	1299	76.6	no	45.82±0.87	14.76±0.50	60.42±1.00	−0.51±0.01
0414190301	2007.06.25	1381	32.0	no	38.34±0.78	10.41±0.41	48.64±0.88	−0.57±0.01
0414190401	2007.12.08	1465	35.4	no	81.05±1.15	19.37±0.57	100.20±1.28	−0.61±0.01
0414190501	2008.12.09	1649	40.5	yes	115.32±2.14	30.12±1.12	144.31±2.40	−0.59±0.01
0414190601	2009.12.20	1837	31.4	no	62.76±1.01	15.43±0.51	78.01±1.13	−0.61±0.01
0414190701	2010.12.10	2015	35.9	no	46.32±0.86	11.07±0.42	57.27±0.95	−0.61±0.01
0414190801	2011.12.12	2199	42.8	no	43.31±0.84	9.82±0.40	53.02±0.93	−0.63±0.01
0414191001	2012.07.16	2308	25.5	no	37.50±0.78	8.58±0.37	45.99±0.86	−0.63±0.01
0414191101	2015.07.13	2856	70.8	no	32.33±0.72	7.23±0.34	39.48±0.80	−0.63±0.02
0414191201	2016.06.26	3031	65.6	no	53.86±0.93	14.98±0.49	68.69±1.05	−0.56±0.01
0414191301	2017.06.26	3214	65.4	no	29.38±0.69	7.85±0.36	37.14±0.78	−0.58±0.01
0414191401	2018.07.04	3401	63.1	no	23.33±0.62	6.65±0.33	29.91±0.70	−0.56±0.02
0810820101	2019.07.02	3583	67.5	no	21.78±0.60	5.83±0.31	27.54±0.67	−0.58±0.02
0810821501	2020.07.06	3768	67.9	no	24.06±0.63	7.05±0.34	31.03±0.71	−0.55±0.02
0810821601	2021.06.09	3938	57.7	no	17.86±0.54	4.89±0.28	22.69±0.61	−0.57±0.02

Notes: ^a GTI = good time interval, ^b μ = mean count rate

between 18.0 and 88.6 ks and were taken over an ~ 21 year time span: the earliest pointed observation was taken on 2000 June 13 and the last one on 2021 June 9. These observations gave us an excellent opportunity to study the flux and spectral variability of the FSRQ blazar 3C 273 on IDV timescales over an extended period. The LCs in all the three bands are plotted; examples are shown in Figs. 1 and 2 and the all LCs are in the online Supplemental Material. Few of these LCs show obvious significant variability over these timescales, which range from 5 to 24.6 hr, so they must be analysed carefully to explore any variations.

3 ANALYSIS TECHNIQUES

In this section, we introduce the analysis methods used to evaluate various quantities characterizing this X-ray data from the blazar 3C 273. The results we obtained are reported in section 4.

3.1 Excess and Fractional Variance

To measure the strength of blazar variability in X-ray bands the commonly used parameters are excess variance σ_{XS}^2 , and fractional rms variability amplitude F_{var} (e.g., [Edelson et al. 2002](#)). Excess variance provides the intrinsic variance of the source by removing the variance due to measurement errors in each individual flux measurement and fractional variance gives the mean variability amplitude with respect to the mean flux of the source. When the LC contains the total number n of flux measurements x_i at times t_i with corresponding errors in measurements $\sigma_{err,i}$, and mean \bar{x} , then the excess

variance is given by

$$\sigma_{XS}^2 = S^2 - \bar{\sigma}_{err}^2, \quad (1)$$

where $\bar{\sigma}_{err}^2$ is the mean square error and S^2 is the sample variance of the LC (for details see [Edelson et al. 2002](#); [Dhiman et al. 2021](#)).

The fractional variance is given by

$$F_{var} = \sqrt{\frac{S^2 - \bar{\sigma}_{err}^2}{\bar{x}^2}} \quad (2)$$

and error in fractional variance is given by (e.g. [Vaughan et al. 2003](#))

$$(F_{var})_{err} = \sqrt{\left[\sqrt{\frac{1}{2n}} \frac{\bar{\sigma}_{err}^2}{F_{var} \bar{x}^2} \right]^2 + \left[\sqrt{\frac{\bar{\sigma}_{err}^2}{n}} \frac{1}{\bar{x}} \right]^2} \quad (3)$$

The values of excess and fractional variances for the soft, hard, and total X-ray bands are given in Table 2.

3.2 Variability Timescale

We use the method for estimating variability timescales as described in ([Bhatta et al. 2018](#); [Zhang et al. 2019](#)). As explained in [Burbidge et al. \(1974\)](#), the timescale of variability of the flux is given by

$$\tau_{var} = \left| \frac{\Delta t}{\Delta \ln \frac{F_1}{F_2}} \right|, \quad (4)$$

where Δt is the time interval between the flux measurements F_1 and F_2 with $F_1 > F_2$. The error in the τ_{var} is given by the formula

Table 2. X-Ray variability parameters in soft, hard and total bands of 3C 273.

Observation ID	F_{var} (percent)								$ \tau ^c(k\text{s})$	$ \tau ^d_{corr}(k\text{s})$	$ \tau ^c(k\text{s})$	$ \tau ^c(k\text{s})$
	Soft (0.2-2 keV)	Sig ^a	Var ^b	Hard (2-10 keV)	Sig ^a	Var ^b	Total (0.2-10 keV)	Sig ^a	Var ^b	Total (0.2-10 keV)	Soft (0.2-2 keV)	Hard (2-10 keV)
0126700301	0.85±0.15	5.67	V	0.17±2.74	0.06	NV	0.64±0.15	4.21	NV	—	1.06±0.31	—
0126700601	0.19±0.88	0.22	NV	0.25±2.81	0.09	NV	0.28±0.48	0.59	NV	—	—	—
0126700701	0.65±0.28	2.32	NV	0.80±0.92	0.87	NV	0.73±0.21	3.43	NV	—	—	—
0126700801	0.94±0.16	5.88	V	1.46±0.40	3.65	NV	0.95±0.13	7.31	V	1.27±0.41	1.09±0.35	1.16±0.38
0136550101	0.87±0.10	8.70	V	0.43±0.79	0.54	NV	0.71±0.10	7.31	V	1.48±0.48	1.28±0.42	1.40±0.48
0159960101	1.30±0.52	2.50	NV	1.49±2.39	0.62	NV	1.12±0.50	2.23	NV	—	—	—
0136550801	0.85±0.29	2.93	NV	1.42±0.81	1.75	NV	0.84±0.25	3.31	NV	—	—	—
0136551001	0.38±0.43	0.88	NV	0.24±2.78	0.09	NV	0.25±0.51	0.49	NV	—	—	—
0414190101	0.92±0.12	7.67	V	1.82±0.20	9.10	V	1.19±0.08	14.10	V	1.40±0.45	1.21±0.39	1.01±0.27
0414190301	0.75±0.25	3.00	NV	0.46±1.33	0.35	NV	0.61±0.23	2.65	NV	—	—	—
0414190401	0.47±0.18	2.62	NV	0.51±0.65	0.78	NV	0.51±0.14	3.65	NV	—	—	—
0414190501	3.19±0.10	31.9	V	2.50±0.27	9.26	V	3.04±0.09	34.26	V	1.17±0.32	1.01±0.28	1.09±0.32
0414190601	0.53±0.22	2.41	NV	1.35±0.37	3.65	NV	0.73±0.14	5.13	V	1.58±0.51	1.36±0.44	—
0414190701	0.53±0.22	2.41	NV	0.91±0.63	1.44	NV	0.83±0.15	5.46	V	1.29±0.39	1.11±0.34	—
0414190801	1.71±0.12	14.25	V	3.84±0.25	15.36	V	2.07±0.10	20.95	V	1.49±0.55	1.29±0.48	1.11±0.34
0414191001	0.30±0.66	0.45	NV	0.75±1.16	0.65	NV	0.22±0.73	0.30	NV	—	—	—
0414191101	1.04±0.15	6.93	V	1.40±0.46	3.04	NV	1.08±0.13	8.52	V	1.13±0.37	0.98±0.32	1.03±0.34
0414191201	0.49±0.18	2.72	NV	0.70±0.45	1.56	NV	0.53±0.14	3.87	NV	—	—	—
0414191301	0.29±0.53	0.55	NV	2.31±0.31	7.45	V	0.68±0.20	3.47	NV	—	—	0.48±0.16
0414191401	0.95±0.23	4.13	NV	1.05±0.69	1.52	NV	0.85±0.20	4.18	NV	—	—	—
0810820101	0.48±0.43	1.12	NV	0.75±1.04	0.72	NV	0.36±0.46	0.78	NV	—	—	—
0810821501	1.79±0.14	12.78	V	2.09±0.36	5.81	V	1.87±0.12	16.09	V	1.00±0.33	0.86±0.28	0.84±0.26
0810821601	0.83±0.35	2.37	NV	1.04±0.99	1.05	NV	0.72±0.31	2.29	NV	—	—	—

 F_{var} = fractional variance^a = Significance (Sig) = $F_{var}/(F_{var})_{err}$ ^b = Variable (Var) = V = variable, NV = non-variable^c = $|\tau|$ = observed halving/doubling time-scale in ks.^d = $|\tau|_{corr}$ = Redshift corrected halving/doubling time-scale: $|\tau|_{corr} = |\tau|/(1+z)$

Zhang et al. (2019)

$$\Delta\tau_{var} \approx \sqrt{\frac{F_1^2 \Delta F_2^2 + F_2^2 \Delta F_1^2}{F_1^2 F_2^2 (\ln[F_1/F_2])^4}} \Delta t \quad (5)$$

Here F_1 and F_2 are the count rates used to estimate the shortest variability timescales and ΔF_1 and ΔF_2 are their corresponding uncertainties. As described in Hagen-Thorn et al. (2008), for a given observation, F_1 and F_2 are chosen in such a way that $|F_i - F_j| > \sigma_{F_i} + \sigma_{F_j}$ where σ_F is the error in flux measurement. The minima of all such pairs $\tau = \min\{\tau_{ij}\}$, where $i = 1, \dots, N-1, j = i+1, \dots, N$ and N is the number of flux values, is the value of the shortest variability timescale. The variability timescale values are given in Table 2.

3.3 Power Spectral Density

The power spectral density (PSD) provides the distribution of variability power as a function of temporal frequency and typically displays a red-noise character at lower frequencies, transitioning to white-noise at higher frequencies where measurement errors dominate.

We compute the PSD using the *periodogram* routine in *python* where the normalization used to plot the periodogram is $(\text{rms}/\text{mean})^2 \text{ Hz}^{-1}$. Then, we fit the periodogram data using maximum likelihood estimation. As discussed in Vaughan (2010), the best fitting model parameter θ is evaluated by maximizing the likelihood function. This is done by minimizing the following fit statistic:

$$S = 2 \sum_{j=1}^{N/2} \frac{I_j}{P_j} + \ln P_j \quad (6)$$

where S is the twice the negative of the log-likelihood and I_j and P_j are the observed periodogram and model spectral density at Fourier frequency ν_j , respectively. Confidence intervals on each model parameter correspond to 68.3% (1 σ). A significant QPO may

be present whenever a peak rises at least by 3σ (99.73%) above the red noise level of the PSD. In the literature, a power-law model has been used to fit PSDs of the LCs in the X-ray and other bands (e.g. González-Martín & Vaughan 2012; Mohan & Mangalam 2015). The power-law form we used is given by

$$P(\nu) = N\nu^{-\alpha} + C, \quad (7)$$

where N is the power-law normalization, α is the spectral index, and C is the additive constant accounting for Poisson noise. We take the value of C as a free parameter that is used for fitting the data. The power-law PSD fits are discussed in Section 4.4.

3.4 Discrete Correlation Function

We use the standard formula for the unbinned discrete correlation function (UDCF) between the hard and soft counts (Edelson & Krolik 1988; Hufnagel & Bregman 1992)

$$UDCF_{ij} = \frac{(x_i - \bar{x})(y_i - \bar{y})}{\sqrt{\sigma_x^2 \sigma_y^2}}. \quad (8)$$

Here x_i and y_i are hard and soft data points, and \bar{x} , \bar{y} , σ_x , σ_y are their means and standard deviations, respectively. Each of the values is associated with a pair-wise lag $t_{ij} = t_j - t_i$. After calculating the UDCF, the DCF at a time-lag τ , where $\tau - \frac{\delta\tau}{2} \leq \delta t_{ij} \leq \tau + \frac{\delta\tau}{2}$ is given by

$$DCF(\tau) = \frac{1}{M} \sum UDCF_{ij} \quad (9)$$

with a bin value M selected as 10. The error is defined as

$$\sigma_{DCF}(\tau) = \frac{\sqrt{\sum (UDCF_{ij} - DCF(\tau))^2}}{M-1} \quad (10)$$

In general, a positive DCF peak means the two data sets are correlated, negative means they are anti-correlated and no DCF peak or DCF = 0 means no correlation exists between the two data sets. The correlation results are discussed in Section 4.5.

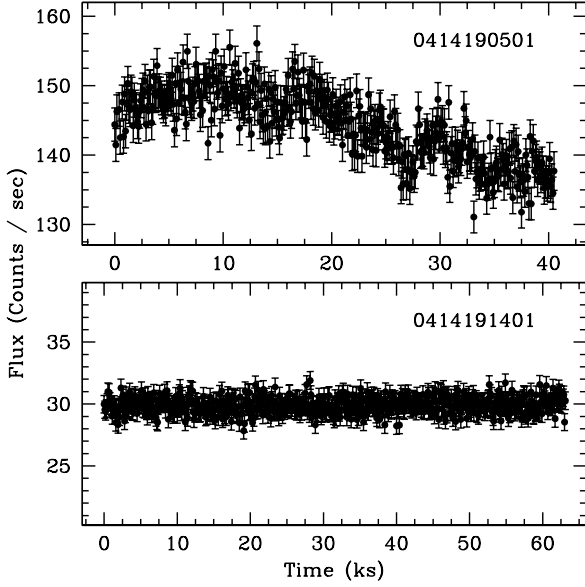


Figure 1. A sample *XMM-Newton* observation ID 0414190501 (variable) and observation ID 0414191401 (non variable) LCs of the blazar 3C 273 in the total (0.2 – 10 keV) energy band, labelled with its observation ID. The LCs for all observations appear in online supplemental material.

3.5 Hardness Ratio

The hardness ratio (HR) is defined as

$$HR = \frac{(H - S)}{(H + S)} \quad (11)$$

where H and S are, respectively, the net count rates in the hard and soft bands. The error on this quantity, σ_{HR} is calculated as (e.g. Zhang et al. 2021)

$$\sigma_{HR} = \frac{2}{(H + S)^2} \sqrt{(H^2 \sigma_S^2 + S^2 \sigma_H^2)}. \quad (12)$$

HR provides a simple and model independent way to study the spectral variability of a source. The HR plot for the Obs IDs we have examined are shown in Fig. 3 and in the Supplemental Material.

3.6 Duty Cycle

The duty cycle (DC) is the fraction of time when an object displays variability. We have estimated the DC of X-ray variability in 3C 273 using the approach given in Romero et al. (1999) and commonly followed thereafter. For calculations of the DC, only those LCs that were continuously monitored for at least 6 hours were considered. The formula is

$$DC = 100 \frac{\sum_{i=1}^n N_i (1/\Delta t_i)}{\sum_{i=1}^n (1/\Delta t_i)} \%, \quad (13)$$

where $\delta t_i = \delta t_{i,obs}(1+z)^{-1}$ is the redshift corrected GTI of the source observed having the i^{th} Obs ID, and N_i takes the value 1 whenever IDV is detected, and 0 when it is not. For a particular Obs ID, if the F_{var} is greater than 5 times the value of $(F_{var})_{err}$, then we consider the LC to show genuine IDV and the N value is taken as 1, as noted in Table 2.

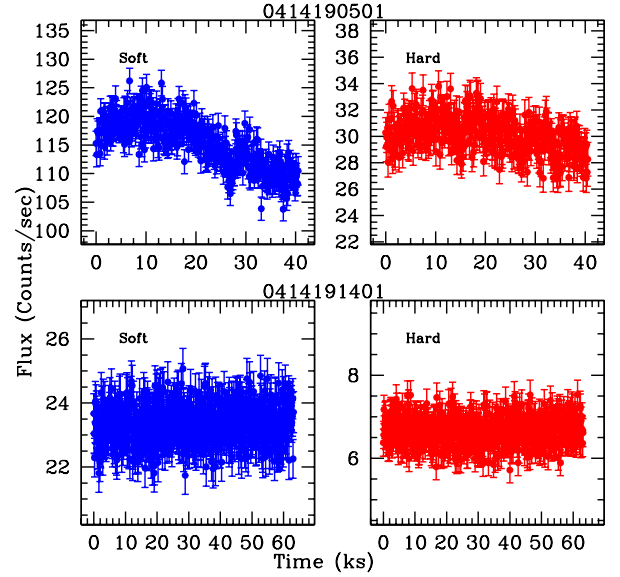


Figure 2. Soft energy (0.2 - 2 keV, upper left plot) and hard energy (2 - 10 keV, upper right plot) LCs for the blazar 3C 273 for a sample *XMM-Newton* observation ID 0414190501 (variable). The similar plots are presented in the lower panels for observation ID 0414191401 (non variable) LCs. The LCs for all observations appear in online supplemental material.

4 RESULTS

By applying the various analysis methods described in Section 3 to the *XMM-Newton* data listed in Table 1, we obtain the following results.

4.1 Intraday Flux Variability

We generated X-ray LCs of individual observation IDs with these 23 observations using three *XMM-Newton* EPIC-pn energy bands (soft, hard, and total). Exemplary LCs of observation IDs 0414190501 (variable) (top panel) and 0414191401 (non variable) (bottom panel) in the total energy (0.2 – 10 keV) band are shown in Fig. 1; the corresponding soft (0.2 – 2.0 keV) and hard (2 – 10 keV) bands are shown in Fig. 2. All 23 LCs are displayed in online supplemental material.

To investigate the flux variability of the blazar 3C 273 on IDV timescales and estimate the variability amplitudes, we have followed the excess variance method explained in Section 3.1 and the obtained results are reported in Table 2. We consider a LC is variable when $F_{var} > 5 \times (F_{var})_{err}$. Using this method, out of 23 LCs in each soft (0.2 – 2 keV), hard (2 – 10 keV), and total (0.2 – 10 keV) energies, we found that 8, 5, and 9 LCs show IDV, respectively. Both well defined increase and decrease in flux within a single observation and rising or falling trends spanning the observation are included with this definition of IDV. We estimated F_{var} and its error for the soft, hard and total bands for all individual Obs IDs and these are reported in Table 2. We also report there the variability time scales, as defined in section 3.2, for all the LCs showing IDV in soft, hard and total energy bands.

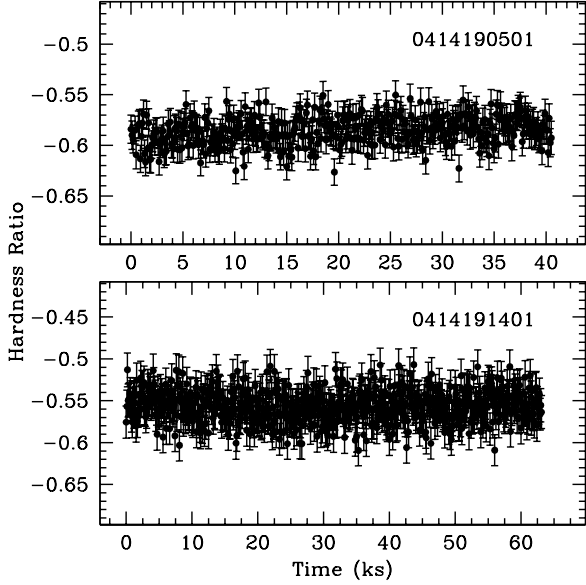


Figure 3. Hardness ratio plot for soft energy (0.2 – 2 keV) and hard energy (2 – 10 keV) for LCs for the blazar 3C 273 for a sample *XMM-Newton* observation ID 0414190501 (variable LCs) and observation ID 0414191401 (non variable LCs). The hardness ratio plots for all observations appear in the online supplement material.

4.2 Intraday Spectral Variability

The hardness ratio (HR) is the simplest and a valuable model independent tool to represent the spectral variations of X-ray emission. The HR with respect to time for exemplary observation IDs 0414190501 (for variable LCs) (top panel) and 0414191401 (for non variable LCs) (bottom panel) are plotted in Fig. 3. All 23 HRs for individual Obs IDs are displayed in online supplemental material. We found no significant changes in HR with respect to time for any of these 23 LCs, which is not surprising since these LCs never showed large amplitudes of variability.

4.3 Duty cycle

We estimated the X-ray variability DC of 3C 273 using the method mentioned in Section 3.6. By considering F_{var} in comparison to its errors to define variability we took the value of $N_i = 1$ if variable, or 0 if not. In the soft (0.2 – 2 keV) and hard (2 – 10 keV) energies, 6 out of 23 and 5 out of 23 LCs, respectively, exhibited variability. But in the total X-ray energy range (0.2 – 10 keV) where the count rates are higher, 9 out of 23 observations were variable. Using this method we found that the X-ray DC of 3C 273 during 2000 – 2021 to be ~ 26 per cent, ~ 22 per cent and ~ 39 per cent in the soft, hard and total energy bands, respectively. However, only 4 out of these 23 Obs IDs have shown clear variations in all three energy bands.

4.4 Intraday Power Spectral Density Analysis

In a major analysis of a large sample of X-ray LCs of various subclasses of AGNs, it was confirmed that the power spectral densities (PSDs) are red-noise dominated that decreases steeply over a range of frequencies as a power-law $P(\nu) \sim \nu^{-\alpha}$ (where ν is temporal frequency), typically with spectral index $\alpha \approx 2$ (González-Martín & Vaughan 2012). Below some particular frequency ν_b (bend

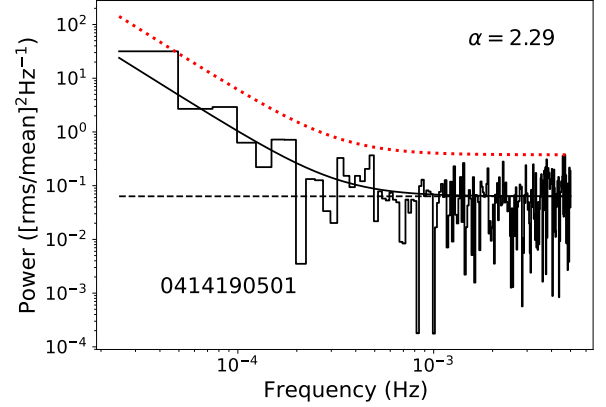


Figure 4. Power spectral density plot of the LC for a sample *XMM-Newton* observation ID 0414190501 (variable LC) in the soft energy band. The observational ID and power spectral index are given in the plot. The continuous line shows the power-law fit to the red noise and the red dotted line shows a level 3σ above the red noise level. PSD plots for all observations appear in online supplement material.

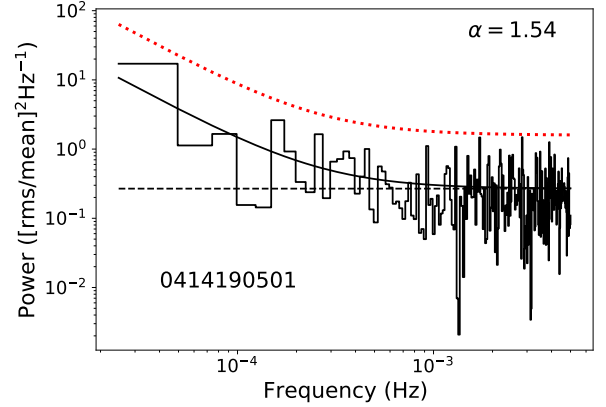


Figure 5. Power spectral density plot of the LC for a sample *XMM-Newton* observation ID 0414190501 (variable LC) in the hard energy band. The observational ID and power spectral index are given in the plot. The continuous line shows the power-law fit to the red noise and the red dotted line shows a level 3σ above the red noise level. PSD plots for all observations appear in online supplement material.

frequency), the PSDs flatten, and these ν_b values scale approximately inversely with the SMBH mass for AGN (González-Martín & Vaughan 2012). Here we characterize the PSDs slopes of the blazar 3C 273 for all nights on which it showed IDV in soft, hard, and total energies taken by *XMM-Newton* over the course of its whole operational period. The resulting fit parameters are given in Table 3, where the slopes and normalization for the power-law red-noise portion of the PSD are given before the flattening to white-noise at the highest frequencies. These power-law fits, to the PSDs observation ID 0414190501 are shown for soft, hard, and total bands in Figures 4 – 6, respectively. The PSDs from all the Obs IDs with detected variability during the course of an observation are displayed in the online supplemental material. We see no evidence for a QPO in any of these PSDs.

In Fig. 7 we have plotted the PSD indices, α , against the fluxes for the 4 Obs IDs in which soft, hard and total X-ray energies are all variable. These points appear show a trend in the sense

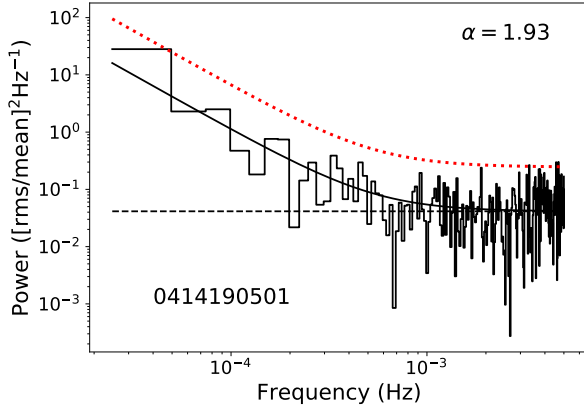
Table 3. Parameters of the power law fits to the PSDs in soft, hard and total bands of 3C 273.

ObsID	Soft (0.2-2 keV)		Hard (2-10 keV)		Total (0.2-10 keV)	
	$\log_{10} N$	α	$\log_{10} N$	α	$\log_{10} N$	α
0126700301	—	—	NV	NV	NV	NV
0126700601	NV	NV	NV	NV	NV	NV
0126700701	NV	NV	NV	NV	NV	NV
0126700801	-6.33 ± 0.29	1.43 ± 0.06	NV	NV	-7.64 ± 0.44	1.71 ± 0.09
0136550101	-12.99 ± 0.55	2.77 ± 0.11	NV	NV	-12.38 ± 0.63	2.61 ± 0.13
0159960101	NV	NV	NV	NV	NV	NV
0136550801	NV	NV	NV	NV	NV	NV
0136551001	NV	NV	NV	NV	NV	NV
0414190101	-10.88 ± 0.40	2.38 ± 0.08	-9.22 ± 0.40	2.13 ± 0.08	-8.81 ± 0.42	1.96 ± 0.09
0414190301	NV	NV	NV	NV	NV	NV
0414190401	NV	NV	NV	NV	NV	NV
0414190501	-9.19 ± 0.61	2.29 ± 0.13	-6.09 ± 0.61	1.54 ± 0.13	-7.67 ± 0.93	1.93 ± 0.20
0414190601	NV	NV	NV	NV	-10.92 ± 1.18	2.44 ± 0.26
0414190701	NV	NV	NV	NV	-8.13 ± 0.88	1.80 ± 0.20
0414190801	-12.00 ± 0.85	2.79 ± 0.18	-11.54 ± 0.85	2.85 ± 0.10	-11.37 ± 0.61	2.69 ± 0.13
0414191001	NV	NV	NV	NV	NV	NV
0414191101	—	—	NV	NV	-6.77 ± 0.26	1.52 ± 0.05
0414191201	NV	NV	NV	NV	NV	NV
0414191301	NV	NV	-13.66 ± 1.06	3.12 ± 0.22	NV	NV
0414191401	NV	NV	NV	NV	NV	NV
0810820101	NV	NV	NV	NV	NV	NV
0810821501	-12.57 ± 0.53	2.84 ± 0.11	-10.52 ± 0.55	2.48 ± 0.11	-11.67 ± 0.27	2.67 ± 0.06
0810821601	NV	NV	NV	NV	NV	NV

Note: N is the normalization and α is the spectral index

— indicates the variations were too small to compute a PSD

NV indicates that the observation is non-variable

**Figure 6.** Power spectral density plot of the LC for a sample *XMM-Newton* observation ID 0414190501 (variable LC) in the total energy band. The observational ID and power spectral index are given in the plot. The continuous line shows power-law fitting of the red noise and the red dotted line shows a level 3σ above the red noise level. PSD plots for all observations appear in online supplement material.

that the brighter sources have shallower PSD slopes. We fitted the straight line in PSD index α versus flux plots in soft, hard and total energies for these 4 obs IDs and in Table 4 where we provide slope, correlation coefficients and probabilities for the null

Table 4. Spectral index versus flux correlation parameters for soft, hard and total X-ray energies.

Energy band	Slope	Correlation coefficient	p-value
Soft	-0.005 ± 0.004	0.451	0.328
Hard	-0.051 ± 0.020	0.766	0.125
Total	-0.009 ± 0.006	0.498	0.294

hypothesis (p -value). However, there are too few data points for any conclusions to be drawn about any trend.

4.5 Intraday Cross-correlated Variability

The relationship between X-ray fluxes in the soft and hard bands is shown in Fig. 8. The plot shows a tight correlation with correlation coefficient 0.953 and probabilities for the null hypothesis (p -value) of 2.3×10^{-12} . This reflects the fact that the HR values changed little between the observations as well as during each one. Such tight correlation between the soft and hard X-ray bands supports the hypotheses that these photons originate from the same regions and are emitted from the same population of leptons. Even stronger support for that likely situation could come from tight cross-correlations between the soft and hard X-ray bands in each individual observation at a very small temporal lag. To test this we performed DCF analyses between these two bands; however, several of the LCs do not show any genuine variability, and when variability is detected, the vari-

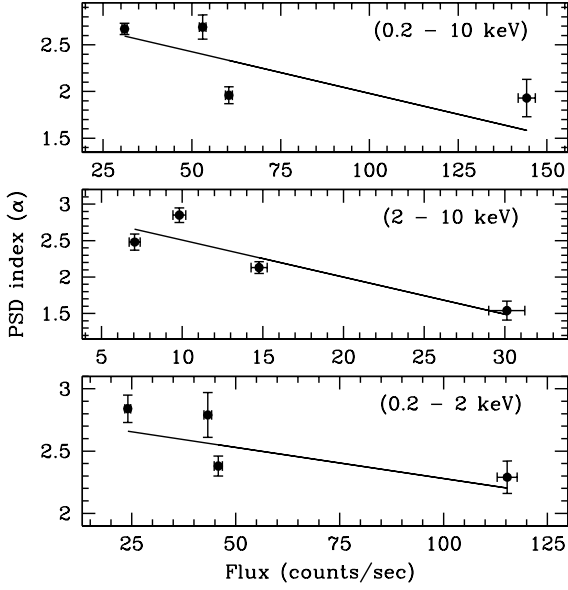


Figure 7. PSD spectral index versus flux plots of the 4 Obs ids which have shown IDV in all soft, hard, and total X-ray energies are plotted with filled circles and straight line fits to possible trends.

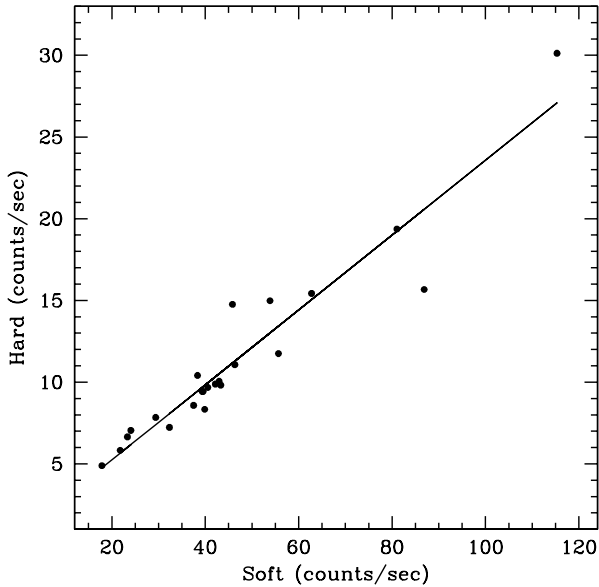


Figure 8. Hard energy flux versus soft energy flux plot for all the observations of the blazar 3C 273.

ability amplitude is usually small. So this analysis only produced poor and irregular DCF plots which are unlikely to indicate real correlations. Similar results were also reported for some of the common *XMM-Newton* observation IDs of 3C 273 reported previously (Kalita et al. 2015).

4.6 Long-term Flux and Spectral Variability

These pointed observations of the blazar 3C 273 were carried out by *XMM-Newton* on many occasions over more than two decades.

These observations provide us an excellent opportunity to study its X-ray flux and spectral variability on LTV timescales. The overall variation in the total X-ray flux with respect to time is shown in the top panel of Fig. 9. On visual inspection we notice that there appears to be a weak trend of decreasing flux with respect to time. There is however, one particularly high X-ray flux point, marked by a red square, that can be considered as an outlier. We computed a least-square fit to these long term data of flux against time, excluding that outlier, which yields a slope of $-1.4 \text{ counts s}^{-1} \text{ yr}^{-1}$ with a correlation coefficient of the fit of -0.487 and a corresponding null hypothesis of 0.0216 . This least-square fit result allows us to say that there is indeed a weak decreasing trend in the flux with time.

The HR (overall spectral change) with time over the entire duration of these observations is presented in the bottom panel of Fig. 9. On visual inspection we notice that there is weak trend of increasing HR with respect to time. One high value HR point is considered as an outlier and marked by red square. The least-square fit to these long term data of HR versus time (excluding the outlier) results in a slope of $3 \times 10^{-3} \text{ yr}^{-1}$ which indicates a decline of 0.06 over ~ 21 years, with correlation coefficient of the fit of 0.631 and its corresponding null hypothesis of 0.0016 . With these least-square fit results, we can say that there is a weak increasing trend in the HR with time on this long timescale. Together, the panels of Fig. 8 indicate an anti-correlation in flux and HR, or a harder-when-brighter trend. This confirms the result found in (Kalita et al. 2015) for the data taken during 2000 – 2015.

In Fig. 10, we present plots of HR against flux of the blazar 3C 273 for six temporal intervals. Spectral evolution of 3C 273 during ≈ 21 years of observation can be interpreted in terms of the changing relative importances of particle acceleration and synchrotron cooling processes in X-ray emitting regions (Kalita et al. 2015). In Fig. 10, we note indications of anticlockwise loops (hard lag) in epochs 2, 3, 4 and partially in epochs 5 and 6. The anticlockwise loops represent that during these epochs of observations the mechanism dominating emission is particle acceleration (e.g., Zhang et al. 2002, and references therein). In epoch 1 and arguably in parts of epochs 5 and 6 clockwise loops (soft lags) are seen in Fig. 10; this can be understood as time when the synchrotron cooling mechanism is dominant. Similar results were found for a subset of these observations of 3C 273 from *XMM-Newton* (Kalita et al. 2015), as well as for Mrk 421 from *Chandra* (Aggarwal et al. 2018), and PKS 2155-304 from *Suzaku* (Zhang et al. 2021).

5 DISCUSSION

We have studied the 23 longest archival pointed observations of the FSRQ blazar 3C 273 taken during 2000 to 2021 by the EPIC-pn instrument on board *XMM-Newton*. These observations were carried out with GTIs from 18.0 to 88.6 ks. We aimed to study flux and spectral variability, cross-correlated variability, and PSDs analysis on IDV timescales for this blazar.

In a series of ten *XMM-Newton* observations in which four are in common with the present study, the soft excess component was found to vary, and could be well fitted by multiple black body components, with temperatures ranging between ~ 40 and ~ 330 eV, together with a power-law (Page et al. 2004). By using quasi-simultaneous *INTEGRAL* and *XMM-Newton* monitoring of the blazar 3C 273 in 2003 – 2005 the $0.2 - 100$ keV spectrum of the

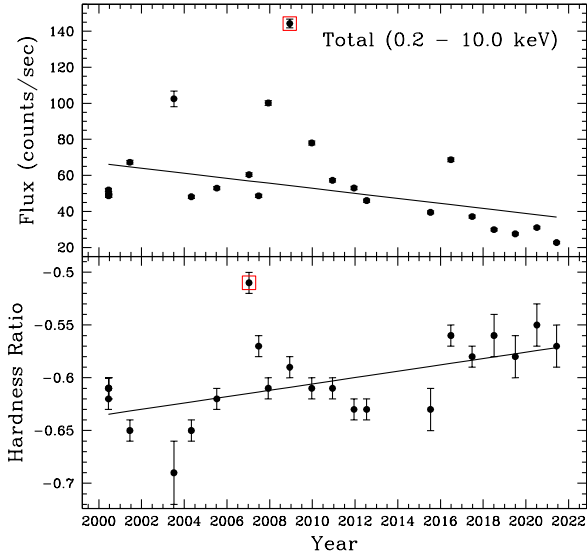


Figure 9. Long term X-ray flux variability (top panel) and spectral variability (bottom panel) of 3C 273.

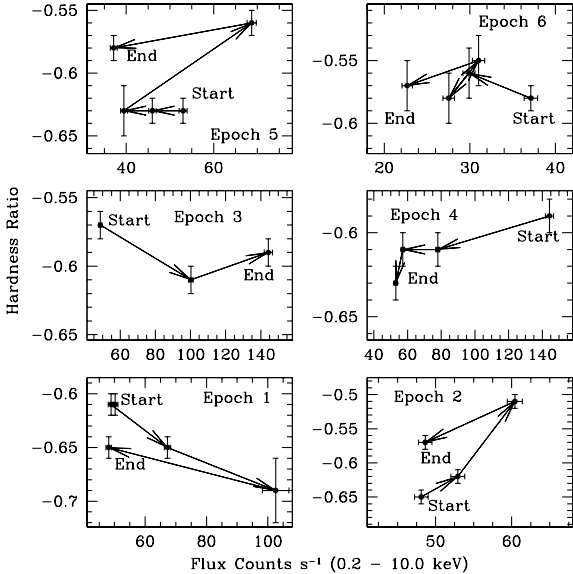


Figure 10. Spectral variations of 3C 273 in different epochs with start and end points marking the loop directions. Each epoch corresponds to the time interval during which the data were considered from Epoch 1 to Epoch 6: Epoch 1: 2000 June 13 to 2004 June 30; Epoch 2: 2004 June 30 to 2007 June 25; Epoch 3: 2007 June 25 to 2008 December 9; Epoch 4: 2008 December 9 to 2011 December 12; Epoch 5: 2011 December 12 to 2017 June 26; and Epoch 6: 2017 June 26 to 2021 June 9.

source was well fitted by a combination of a soft cut-off power-law and a hard power-law and the source reached its historically softest state in the hard X-ray domain with a photon index $\Gamma = 1.82 \pm 0.01$ (Chernyakova et al. 2007). There were 3 common Obs IDs of *XMM-Newton* in the present study and that of Chernyakova et al. (2007).

Multi-band X-ray, UV and optical observations of 3C 273 including data from *XMM-Newton* were used to study flux, spectral and cross-correlated variabilities on diverse timescales. Long-term observations of 3C 273 found that IDV X-ray LCs showed small amplitude variability, along with large amplitude variability in optical to X-ray energies on longer timescales, an anti-correlation in UV and X-ray emission in a low flux state, and a harder-when-brighter trend for the X-ray spectrum (Kalita et al. 2015; Kalita et al. 2017). There are 16 Obs IDs studied in the present paper that are also considered in those papers (Kalita et al. 2015; Kalita et al. 2017). González-Martín & Vaughan (2012) have studied PSD properties of 104 AGN including 3C 273 using *XMM-Newton* observations, including 6 common Obs IDs studied in the present paper and in that one. The PSD results of González-Martín & Vaughan (2012) and in the present study for common Obs IDs are consistent.

Therefore, the modest X-ray variability seen in 3C 273 seen on these timescales might arise from the jet or accretion disc coronal emission, or a combination of both. Characteristics of such variations, particularly their PSDs, might be used to distinguish between those possibilities. While there have now been a substantial number of jet and disc simulations, including some very sophisticated general relativistic magnetodynamical computations including radiation transport that include disc, corona, and the innermost portion of a jet (e.g., Burke et al. 2021) only a very small subset of them carry these simulations far enough to yield light curves and then compute their power-spectra. As summarized in Wehrle et al. (2019) accretion disc models that do so typically produce PSD slopes in the range $1.3 \lesssim \alpha \lesssim 2.1$, though it is possible to see somewhat steeper PSDs for some geometries. On the other hand, jet based models more typically yield somewhat steeper PSD slopes $1.7 \lesssim \alpha \lesssim 2.9$, although these simulations have typically probed timescales from weeks to years. The observed PSD slopes found here ($1.43 \leq \alpha \leq 3.12$) for the X-ray emission of 3C 273 span both ranges, though the majority of them seem to be more consistent with jet-based simulations. However, given the limited range of the PSDs found in this work and the still small number of computational papers that provide PSDs, we cannot claim more than a tentative hint favouring fluctuations originating in jets.

6 CONCLUSIONS

We studied 23 observations of the FSRQ 3C 273 from the public archive *XMM-Newton*. These EPIC-pn light curves for the blazar were taken during 2000 – 2021. We searched for intraday variability and its timescales, HRs, time lags between soft and hard energies, and also carried out PSD analyses to characterize the IDV and to search for any possible QPO present. Our conclusions are summarized as follows:

- The source showed fractional variabilities of small amplitude 0.71 ± 0.10 per cent to 3.04 ± 0.09 per cent in 9 light curves, while 14 light curves do not show any significant variability in the total X-ray energy band. This indicates a duty cycle of ~ 40 per

cent in the total energy band. No strong flare is seen on any of the observation ID light curve and the typical IDV timescale is found to be ~ 1 ks.

- There is no significant change in spectral variation, as measured by the hardness ratio, seen during any of the observations.
- The relationship between X-ray fluxes in the soft and hard bands shows a tight correlation with correlation coefficient 0.953 and probability for the null hypothesis (p-value) of 2.3×10^{-12} .
- A power-law model gives good fits to each of the PSDs (at lower frequencies) and the slopes range between 1.4 and 3.1 but the vast majority are between 1.7 and 2.8, so steeper than flicker noise. No evidence for any QPOs were seen.
- An anti-correlation in flux and hardness ratio is found in the long term data which implies a harder when brighter trend.
- The flux and spectral analyses indicate that both particle acceleration and synchrotron cooling processes make an important contribution to the emission from this blazar.

ACKNOWLEDGEMENTS

This research is based on observations obtained with *XMM-Newton*, an ESA science mission with instruments and contributions directly funded by ESA member states and NASA. Data from the Steward Observatory spectropolarimetric monitoring project were used. This programme is supported by Fermi Guest Investigator grants NNX08AW56G, NNX09AU10G, NNX12AO93G, and NNX15AU81G.

We thank the anonymous referees for useful comments. HG acknowledges financial support from the Department of Science & Technology (DST), Government of India, through the INSPIRE faculty award IFA17-PH197 at ARIES, Nainital, India. ACG is thankful to Dr. Main Pal for discussion about *XMM-Newton* data analysis. ML is supported by the China Postdoctoral Science Foundation (Grant No. 2021M693089).

DATA AVAILABILITY

The data sets were derived from sources in the public domain: [XMM-Newton, <https://heasarc.gsfc.nasa.gov/db-perl/W3Browse/w3browse.pl>]. The data underlying this article will be shared on reasonable request to the corresponding author.

SUPPORTING INFORMATION

Supplementary data are available at MNRAS online.

Figure 1. All *XMM-Newton* light curves in the total energy range 0.2 – 10 keV of the blazar 3C 273, labelled with its observation IDs in each panel.

Figure 2. All *XMM-Newton* light curves in the soft energy range 0.2 – 2 keV and 2 – 10 keV of the blazar 3C 273, labelled with its observation IDs in each panel.

Figure 3. Hardness ratio plots for all observation IDs of *XMM-Newton* of the blazar 3C 273.

Figure 4. Power spectral density plots of the light curves for all observation IDs of *XMM-Newton* of the blazar 3C 273 in the soft energy band. In the each plot the continuous line shows power-law fitting of the red noise and the red dotted line shows a level 3σ above the red noise level. The observational ID and power spectral index are given in the each plot.

Figure 5. Power spectral density plots of the light curves for all observation IDs of *XMM-Newton* of the blazar 3C 273 in the hard energy band. In the each plot the continuous line shows power-law fitting of the red noise and the red dotted line shows a level 3σ above the red noise level. The observational ID and power spectral index are given in the each plot.

Figure 6. Power spectral density plots of the light curves for all observation IDs of *XMM-Newton* of the blazar 3C 273 in the total energy band. In the each plot the continuous line shows power-law fitting of the red noise and the red dotted line shows a level 3σ above the red noise level. The observational ID and power spectral index are given in the each plot.

REFERENCES

- Abdo A. A. et al., 2010, *ApJ*, 714, L73
 Aggrawal V., Pandey A., Gupta A. C., Zhang Z., Wiita P. J., Yadav K. K., Tiwari S. N., 2018, *MNRAS*, 480, 4873
 Attridge J. M., Wardle J. F. C., Homan D. C., 2005, *ApJ*, 633, L85
 Bhagwan J., Gupta A. C., Papadakis I. E., Wiita P. J., 2014, *MNRAS*, 444, 3647
 Bhagwan J., Gupta A. C., Papadakis I. E., Wiita P. J., 2016, *New Astron.*, 44, 21
 Bhatta G., Mohorian M., Bilinsky I., 2018, *A&A*, 619, A93
 Blandford R. D., Rees M. J., 1978, *Phys. Scr.*, 17, 265
 Borse N., Acharya S., Vaidya B., Mukherjee D., Bodo G., Rossi P., Mignone A., 2021, *A&A*, 649, A150
 Buisson D. J. K., Lohfink A. M., Alston W. N., Fabian A. C., 2017, *MNRAS*, 464, 3194
 Burbidge G. R., Jones T. W., O'Dell S. L., 1974, *ApJ*, 193, 43
 Burke C. J. et al., 2021, *Science*, 373, 789
 Calafut V., Wiita P. J., 2015, *Journal of Astrophysics and Astronomy*, 36, 255
 Carini M., Wehrle A. E., Wiita P. J., Ward Z., Pendleton K., 2020, *ApJ*, 903, 134
 Chakrabarti S. K., Wiita P. J., 1993, *ApJ*, 411, 602
 Chernyakova M. et al., 2007, *A&A*, 465, 147
 Chidiac C. et al., 2016, *A&A*, 590, A61
 Collmar W. et al., 2000, *A&A*, 354, 513
 Courvoisier T. J. L. et al., 2003, *A&A*, 411, L343
 Dhiman V., Gupta A. C., Gaur H., Wiita P. J., 2021, *MNRAS*, 506, 1198
 Edelson R., Turner T. J., Pounds K., Vaughan S., Markowitz A., Marshall H., Dobbie P., Warwick R., 2002, *ApJ*, 568, 610
 Edelson R. A., Krolik J. H., 1988, *ApJ*, 333, 646
 Esposito V., Walter R., Jean P., Tramacere A., Türler M., Lähteenmäki A., Tornikoski M., 2015, *A&A*, 576, A122
 Fan J. H., Kurtanidze O., Liu Y., Richter G. M., Chanishvili R., Yuan Y. H., 2014, *ApJS*, 213, 26
 Fan J. H., Peng Q. S., Tao J., Qian B. C., Shen Z. Q., 2009, *AJ*, 138, 1428
 Fernandes S., Patiño-Álvarez V. M., Chavushyan V., Schlegel E. M., Valdés J. R., 2020, *MNRAS*, 497, 2066
 Gaur H., Gupta A. C., Lachowicz P., Wiita P. J., 2010, *ApJ*, 718, 279
 Ghisellini G. et al., 1997, *A&A*, 327, 61
 González-Martín O., Vaughan S., 2012, *A&A*, 544, A80
 Gopal-Krishna, Wiita P. J., 1992, *A&A*, 259, 109

- Grandi P., Palumbo G. G. C., 2004, *Science*, 306, 998
- Gupta A. C., Banerjee D. P. K., Ashok N. M., Joshi U. C., 2004, *A&A*, 422, 505
- Gupta A. C., Kalita N., Gaur H., Duorah K., 2016, *MNRAS*, 462, 1508
- Hagen-Thorn V. A., Larionov V. M., Jorstad S. G., Arkharov A. A., Hagen-Thorn E. I., Efimova N. V., Larionova L. V., Marscher A. P., 2008, *ApJ*, 672, 40
- Hufnagel B. R., Bregman J. N., 1992, *ApJ*, 386, 473
- Impey C. D., Malkan M. A., Tapia S., 1989, *ApJ*, 347, 96
- Jester S., Harris D. E., Marshall H. L., Meisenheimer K., 2006, *ApJ*, 648, 900
- Jorstad S. G. et al., 2005, *AJ*, 130, 1418
- Jorstad S. G., Marscher A. P., Mattox J. R., Wehrle A. E., Bloom S. D., Yurchenko A. V., 2001, *ApJS*, 134, 181
- Kalita N., Gupta A. C., Wiita P. J., Bhagwan J., Duorah K., 2015, *MNRAS*, 451, 1356
- Kalita N., Gupta A. C., Wiita P. J., Dewangan G. C., Duorah K., 2017, *MNRAS*, 469, 3824
- Kataoka J., Tanihata C., Kawai N., Takahara F., Takahashi T., Edwards P. G., Makino F., 2002, *MNRAS*, 336, 932
- Kellermann K. I., Sramek R., Schmidt M., Shaffer D. B., Green R., 1989, *AJ*, 98, 1195
- Kirk J. G., Rieger F. M., Mastichiadis A., 1998, *A&A*, 333, 452
- Krawczynski H., 2004, *New Astron. Rev.*, 48, 367
- Kundu E., Gupta N., 2014, *MNRAS*, 444, L16
- Lachowicz P., Gupta A. C., Gaur H., Wiita P. J., 2009, *A&A*, 506, L17
- Li Y.-R., Zhang Z.-X., Jin C., Du P., Cui L., Liu X., Wang J.-M., 2020, *ApJ*, 897, 18
- Liu H., Luo B., Brandt W. N., Brotherton M. S., Gallagher S. C., Ni Q., Shemmer O., Timlin, J. D. I., 2021, *ApJ*, 910, 103
- Liu H. T., Feng H. C., Xin Y. X., Bai J. M., Li S. K., Wang F., 2019, *ApJ*, 880, 155
- Magdziarz P., Zdziarski A. A., 1995, *MNRAS*, 273, 837
- Mangalam A. V., Wiita P. J., 1993, *ApJ*, 406, 420
- Marcha M. J. M., Browne I. W. A., Impey C. D., Smith P. S., 1996, *MNRAS*, 281, 425
- Marscher A. P., 2014, *ApJ*, 780, 87
- Marscher A. P., Gear W. K., 1985, *ApJ*, 298, 114
- Marshall H. L. et al., 2001, *ApJ*, 549, L167
- Mohan P., Mangalam A., 2015, *ApJ*, 805, 91
- Mücke A., Protheroe R. J., Engel R., Rachen J. P., Stanev T., 2003, *Astroparticle Physics*, 18, 593
- Padovani P., 2017, *Nature Astronomy*, 1, 0194
- Page K. L., Turner M. J. L., Done C., O'Brien P. T., Reeves J. N., Sembay S., Stuhlinger M., 2004, *MNRAS*, 349, 57
- Paltani S., Courvoisier T. J. L., Walter R., 1998, *A&A*, 340, 47
- Paltani S., Türler M., 2005, *A&A*, 435, 811
- Pandey A., Gupta A. C., Wiita P. J., 2017, *ApJ*, 841, 123
- Pandey A., Gupta A. C., Wiita P. J., 2018, *ApJ*, 859, 49
- Pollack M., Pauls D., Wiita P. J., 2016, *ApJ*, 820, 12
- Romero G. E., Cellone S. A., Combi J. A., 1999, *A&AS*, 135, 477
- Romero G. E., Chajet L., Abraham Z., Fan J. H., 2000, *A&A*, 360, 57
- Röser H. J., Meisenheimer K., Neumann M., Conway R. G., Perley R. A., 2000, *A&A*, 360, 99
- Sambruna R. M., Urry C. M., Tavecchio F., Maraschi L., Scarpa R., Chartas G., Muxlow T., 2001, *ApJ*, 549, L161
- Savolainen T., Wiik K., Valtaoja E., Tornikoski M., 2006, *A&A*, 446, 71
- Schmidt M., 1963, *Nature*, 197, 1040
- Soldi S. et al., 2008, *A&A*, 486, 411
- Stoeckle J. T., Case J., Donahue M., Shull J. M., Snow T. P., 1991, *ApJ*, 374, 72
- Uchiyama Y. et al., 2006, *ApJ*, 648, 910
- Urry C. M., Padovani P., 1995, *PASP*, 107, 803
- Vaughan S., 2010, *MNRAS*, 402, 307
- Vaughan S., F. R., Warwick R. S., Uttley P., 2003, *MNRAS*, 345, 1271
- Wagner S. J., Witzel A., 1995, *ARA&A*, 33, 163
- Wehrle A. E., Carini M., Wiita P. J., 2019, *ApJ*, 877, 151
- Yaqoob T., Serlemitsos P., 2000, *ApJ*, 544, L95
- Zhang H., Giannios D., 2021, *MNRAS*, 502, 1145
- Zhang Y. H. et al., 2002, *ApJ*, 572, 762
- Zhang Z., Gupta A. C., Gaur H., Wiita P. J., An T., Gu M., Hu D., Xu H., 2019, *ApJ*, 884, 125
- Zhang Z., Gupta A. C., Gaur H., Wiita P. J., An T., Lu Y., Fan S., Xu H., 2021, *ApJ*, 909, 103